Chemistry – An Asian Journal

CHEMISTRY AN ASIAN JOURNAL | ACES Asian Chemical Editorial Society

RESEARCH ARTICLE

Functional Group Spatial Arrangement in Cationic Polymeric Nanotraps for Selective Perrhenate Anion Capture

Xiaorui Li[1,2] | Jiahong Yang[1] | Wenping Liu[3] | Haiying Wang[2] | Yu Zhang[3] | Xinhui Deng[1] | Linfeng Jin[1] | Huan Li[1] | Changqing Su[1] | Yiming Li[3] | Thamraa AlShahrani[4] | Shengqian Ma[5]

[1]School of Resource & Environment, Hunan Provincial Key Laboratory of Carbon Neutrality and Intelligent Energy, Hunan University of Technology and Business, Changsha, Hunan, China | [2]School of Metallurgy and Environment, Central South University, Changsha, Hunan, China | [3]College of Chemistry and Chemical Engineering, Central South University, Changsha, Hunan, China | [4]Department of Physics, College of Science, Princess Nourah bint Abdulrahman University, Riyadh, Saudi Arabia | [5]Department of Chemistry, University of North Texas, Denton, Texas, USA

Correspondence: Yiming Li (chemyl@csu.edu.cn) | Shengqian Ma (Shengqian.Ma@unt.edu)

Received: 18 January 2026 | **Revised:** 6 September 2026 | **Accepted:** 12 September 2026

Keywords: cationic polymeric nanotraps | imidazolium | ion exchange | perrhenate anion

ABSTRACT

The selective capture of specific anions from complex wastewater remains a critical challenge in resource recovery. Although cationic polymers can adsorb anions through ion exchange, the influence of the spatial arrangement of the functional group on their selectivity is not well understood. In this study, two imidazolium-based cationic polymers with *ortho*- and *para*-substituted spatial arrangements (denoted as **CPN-oVIm-Cl** and **CPN-pVIm-Cl**) were synthesized, and their efficacy in the selective adsorption of perrhenate was comparatively studied. Both materials exhibit high adsorption capacities for perrhenate, reaching over 1200 mg g^{-1}, along with rapid adsorption kinetics. A key finding is that **CPN-pVIm-Cl** shows significantly superior selectivity toward ReO_4^- in the presence of multicharged competing anions such as SO_4^{2-} and AsO_4^{3-}, compared to **CPN-oVIm-Cl**. Mechanistic studies indicate that the uniformly distributed charges in the *para*-substituted polymer enhance specific recognition, whereas the locally concentrated charges in the *ortho*-substituted analogue reduce selectivity. This work highlights the spatial arrangement of functional groups as a key factor in tuning ion selectivity, offering a new perspective for designing high-performance adsorbents.

1 | Introduction

Rhenium represents an indispensable strategic metal that finds widespread use in cutting-edge technologies, particularly high-temperature alloys for aerospace propulsion and catalysts employed in the petrochemical sector [1, 2]. Nevertheless, the recovery of rhenium poses substantial challenges owing to its ultra-low abundance in the Earth's crust and the absence of standalone mineral deposits [3]. Industrially, rhenium is predominantly obtained as a secondary product during copper and molybdenum smelting operations, in which it occurs as the perrhenate anion (ReO_4^-) within acidic process wastewater [4]. Such effluents constitute a highly complex matrix featuring pronounced acidity, trace-level ReO_4^- concentrations, and an abundance of competing anions. In particular, multivalent species including sulfate (SO_4^{2-}) and arsenate (AsO_4^{3-}) frequently coexist at concentrations several orders of magnitude greater than that of perrhenate [5]. Consequently, adsorbents intended for rhenium recovery must satisfy stringent criteria, including large uptake capacity, outstanding selectivity, and

All rights reserved, including rights for text and data mining and training of artificial intelligence technologies or similar technologies.
© 2026 Wiley-VCH GmbH

durable chemical stability under harsh operating conditions [6].

A wide range of adsorbent platforms has been investigated to meet this challenge, encompassing metal–organic frameworks (MOFs) [7, 8], covalent organic frameworks (COFs) [9], cationic polymers [10, 11], inorganic composites [12], carbon-based materials [13], and other emerging systems [14]. Within this landscape, cationic polymers have attracted considerable attention for anion sequestration through an ion-exchange pathway, benefiting from their tailorable structures, large uptake capacities, and robust chemical stability [10]. By integrating positively charged moieties(such as quaternary ammonium [15], pyridinium [16, 17], or imidazolium salts [18–20]) into a polymeric network, these materials can achieve markedly enhanced affinity and capacity toward target anions. Substantial research efforts have been devoted to the design of new charged building blocks, the exploration of varied polymeric backbones, and the application of sophisticated synthetic methodologies to regulate bulk material properties. By comparison, a fundamental microstructural characteristic has remained largely underexplored: the precise spatial distribution of cationic sites tethered to the polymer backbone. Variations in nanoscale spatial organization can substantially alter the local electrostatic landscape of a material, which in turn dictates its capacity to selectively recognize and sequester specific anions from multicomponent solutions. Accordingly, establishing the structure–performance relationship associated with this parameter is of critical importance for the rational engineering of next-generation selective separation media. Our group previously reported an imidazolium-based cationic polymeric nanotrap for efficient perrhenate capture, which demonstrated high adsorption capacity, broad pH tolerance, and excellent structural stability under acidic conditions [21]. Nevertheless, the influence of functional group spatial arrangement on anion selectivity—a fundamental microstructural parameter that governs ion recognition—has not been systematically investigated in this class of cationic polymeric materials.

In this work, two imidazolium-based cationic polymers bearing *ortho*- and *para*-disubstituted configurations (designated **CPN-oVIm-Cl** and **CPN-pVIm-Cl**) were rationally designed and synthesized to enable a comparative investigation of their performance in the selective uptake of perrhenate from aqueous media. A comprehensive evaluation of their perrhenate adsorption behavior was conducted, encompassing uptake capacity, sorption kinetics, pH adaptability, and reusability. The two polymers possess identical functional group compositions and similar theoretical charge densities, differing exclusively in the relative positioning of the cationic centers on the phenylene bridging unit. This well-controlled structural divergence affords an ideal model system for investigating the impact of functional group spatial arrangement on adsorption selectivity. Closely packed cationic sites produce localized high-charge-density domains that induce unfavorable non-specific binding with multivalent competing anions and reduce the selectivity for monovalent ReO_4^-, whereas uniform charge distribution suppresses such undesired interactions and maintains good ReO_4^- selectivity in complex water matrices. These findings identify functional-group spatial distribution as a critical design parameter for anion selectivity, providing a molecular-level design guidance for the future development of advanced selective adsorbents.

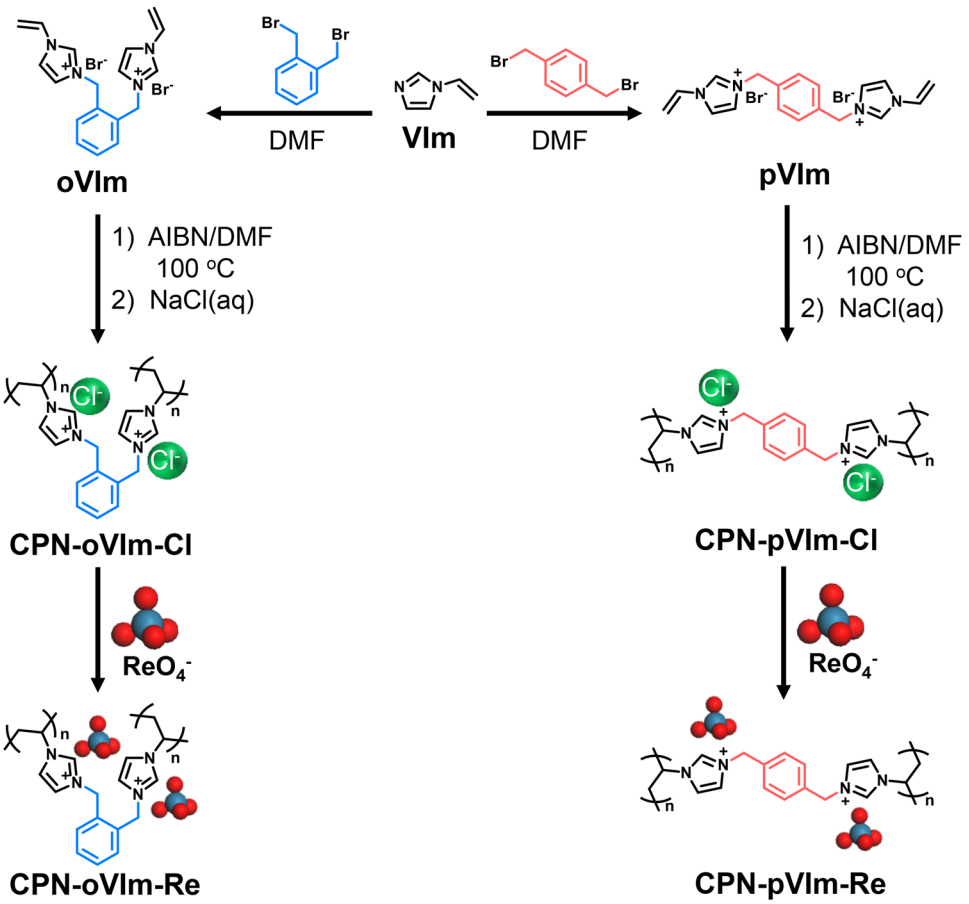
2 | Results and Discussion

2.1 | Synthesis and Characterization

CPN-pVIm-Cl and **CPN-oVIm-Cl** were fabricated following the synthetic pathway depicted in Scheme 1. Initially, two regioisomeric imidazolium salt monomers (*para*-disubstituted **pVIm** and *ortho*-disubstituted **oVIm**) were prepared through a rationally designed molecular synthesis route. Both monomers were then employed as precursors for free-radical polymerization under identical conditions, affording the corresponding bromide-form polymers, **CPN-pVIm-Br** and **CPN-oVIm-Br**, respectively. A subsequent anion-exchange treatment was carried out to improve the sorption kinetics of the resulting materials. Specifically, the as-synthesized bromide-form polymers were immersed in a 2 M aqueous NaCl solution to exchange the Br^- counterions for Cl^- [22], yielding the final chloride-form products, **CPN-pVIm-Cl** and **CPN-oVIm-Cl**.

The chemical integrity of the polymeric networks was initially verified by solid-state ^{13}C NMR spectroscopy. As illustrated in Figure 1a,b, the ^{13}C NMR spectra of both **CPN-oVIm-Cl** and **CPN-pVIm-Cl** display well-resolved resonance signals, and all observed peaks can be unambiguously assigned to the constituent carbon atoms of the polymer backbone through comparison with the corresponding monomer precursors (Figures S1–S4). Taking **CPN-oVIm-Cl** as a representative example (Figure 1a), the resonance at 126.9 ppm is ascribed to the aromatic carbons of the phenylene ring together with the C5 carbon of the imidazolium moiety. A second signal appearing near 117 ppm corresponds to the C3 and C4 carbons of the imidazolium ring. On the basis of a 2:1 integrated area ratio, the resonance centered at approximately 48 ppm is assigned to the C2 and C6 methylene carbons, whereas the signal at 32.0 ppm originates from the C1 carbon [21]. Importantly, no characteristic olefinic resonances attributable to unreacted vinyl groups are detectable in either spectrum, which confirms the successful completion of free-radical polymerization and verifies the formation of the desired cross-linked polymer networks. The peak assignment for **CPN-pVIm-Cl** (Figure 1b) follows an analogous pattern to that of **CPN-oVIm-Cl**, with minor shifts in chemical origin arising from the different substitution geometry on the phenylene linker.

Fourier transform infrared (FT-IR) spectroscopy was employed to further corroborate the presence of the key functional moieties (Figure 4c,e). A broad absorption band spanning the 2900–3200 cm^{-1} region is observable in both spectra, which is assignable to the stretching vibrations of C—H bonds associated with the imidazolium groups and the phenylene rings. The formation of the imidazolium salt structure is evidenced by characteristic absorption bands appearing at approximately 1631 and 1552 cm^{-1}. Furthermore, a well-defined resonance located at 1155 cm^{-1} within the fingerprint region corresponds to the skeletal stretching vibration of the imidazolium framework, in good agreement with previously reported values [21]. The overall spectral profiles of the two polymers are highly similar,



SCHEME 1 | Synthetic route of **CPN-oVIm-Cl**, **CPN-pVIm-Cl** and their anion-exchange process.

consistent with their identical functional group compositions and differing only in the relative spatial arrangement of the cationic centers.

The surface morphologies of the two polymeric materials were examined by scanning electron microscopy (SEM). As depicted in Figure 1c,d, both **CPN-pVIm-Cl** and **CPN-oVIm-Cl** exhibit a rough surface topography consisting of aggregates of irregularly shaped nanoparticles, with no discernible difference in macroscopic morphology between the two regioisomeric polymers. Powder X-ray diffraction (PXRD) analysis provides further insight into their structural characteristics. The PXRD patterns of both polymers display only a broad, diffuse halo centered at approximately 25° (Figure S5), with no sharp diffraction peaks observable. This finding is indicative of the amorphous nature of both materials and confirms the absence of long-range crystalline order within the polymer networks.

The surface hydrophilicity of the resulting polymers was further assessed through water vapor adsorption measurements. Both materials demonstrate a pronounced affinity toward water vapor, as illustrated by their adsorption–desorption isotherms collected at 298 K (Figure 1e). Taking **CPN-oVIm-Cl** as a representative example, the water vapor uptake reaches 185.6 $cm^3\ g^{-1}$ at a relative pressure (P/P_0) of 0.71, while **CPN-pVIm-Cl** displays a similarly shaped isotherm with a comparable uptake capacity. The steep ascent of both isotherms at low relative pressures is indicative of strong hydrophilic interactions between the positively charged polymeric frameworks and water molecules, consistent with the highly charged nature of the imidazolium-based networks.

Given that stability under application-relevant conditions is a critical prerequisite for practical deployment, comprehensive stability evaluations were conducted for both polymeric adsorbents. The thermal stability of the two materials was assessed by thermogravimetric analysis (TGA). As shown in Figure 1f, **CPN-pVIm-Cl** and **CPN-oVIm-Cl** exhibit closely comparable TGA profiles. Both materials experience an initial weight loss of approximately 15% upon heating to 160°C, which is attributed to the evaporation of physisorbed water molecules retained within the hydrophilic polymer networks. Following this initial dehydration step, the polymeric frameworks remain structurally intact up to 250°C, thereby demonstrating good thermal stability. These findings confirm that both **CPN-pVIm-Cl** and **CPN-oVIm-Cl** possess favorable thermal robustness, which supports their potential applicability under realistic industrial operating conditions.

2.2 | Sorption Investigation

With the structural integrity of both polymers confirmed, their perrhenate adsorption performance was systematically evaluated. Adsorption isotherm measurements were initially performed over an initial ReO_4^- concentration range of 10–1000 ppm. As illustrated in Figure 2a,b, the uptake capacities

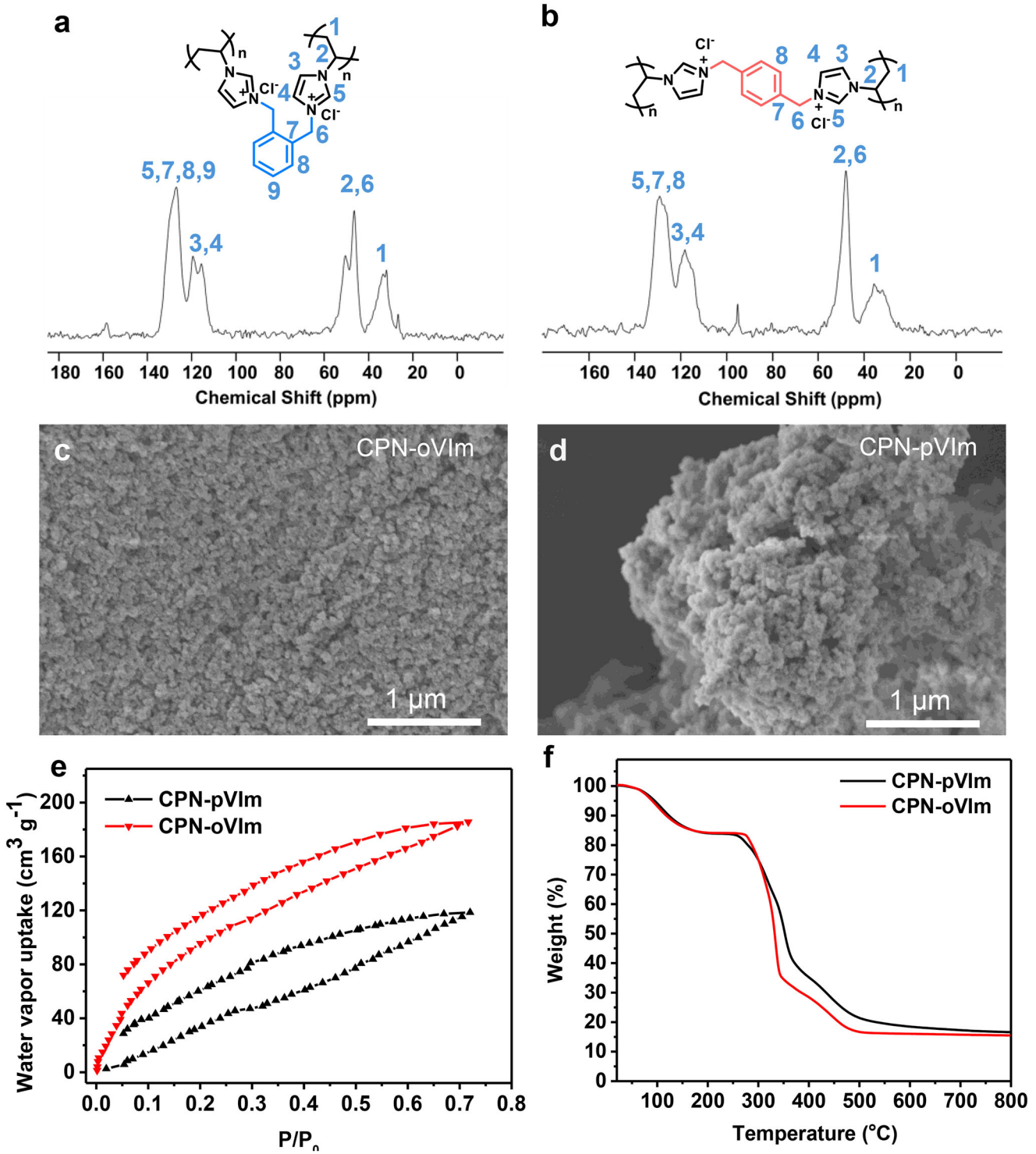


FIGURE 1 | Solid-state ^{13}C NMR spectrum of (a) **CPN-oVIm-Cl** and (b) **CPN-pVIm-Cl**. SEM image of (c) **CPN-oVIm-Cl** and (d) **CPN-pVIm-Cl**. (e) Water vapor adsorption–desorption isotherm of **CPN-oVIm-Cl** and **CPN-pVIm-Cl** at 298 K; P_0 is the saturated vapor pressure of water vapor. (f) TGA of **CPN-pVIm-Cl** and **CPN-oVIm-Cl** under Ar atmosphere.

of both polymers increase monotonically with rising equilibrium concentration, eventually approaching a plateau at higher concentrations. The experimental data were fitted using both the Langmuir and Freundlich isotherm models (insets of Figures 2a,b, and S6). The Langmuir model affords a superior fit to the adsorption data for both materials, as reflected in the higher correlation coefficients ($R^2 > 0.999$ for **CPN-oVIm-Cl** and $R^2 > 0.98$ for **CPN-pVIm-Cl**). A comparative analysis of the fitted Langmuir parameters reveals that **CPN-pVIm-Cl** exhibits a larger Langmuir constant ($K_L = 0.24$ L mg^{-1}) than **CPN-oVIm-Cl** ($K_L = 0.08$ L mg^{-1}), suggesting a stronger intrinsic affinity of the *para*-substituted polymer toward perrhenate anions. The model-derived maximum adsorption capacities are 934.6 mg g^{-1} for **CPN-pVIm-Cl** and 1088.6 mg g^{-1} for **CPN-oVIm-Cl** (Table S1),

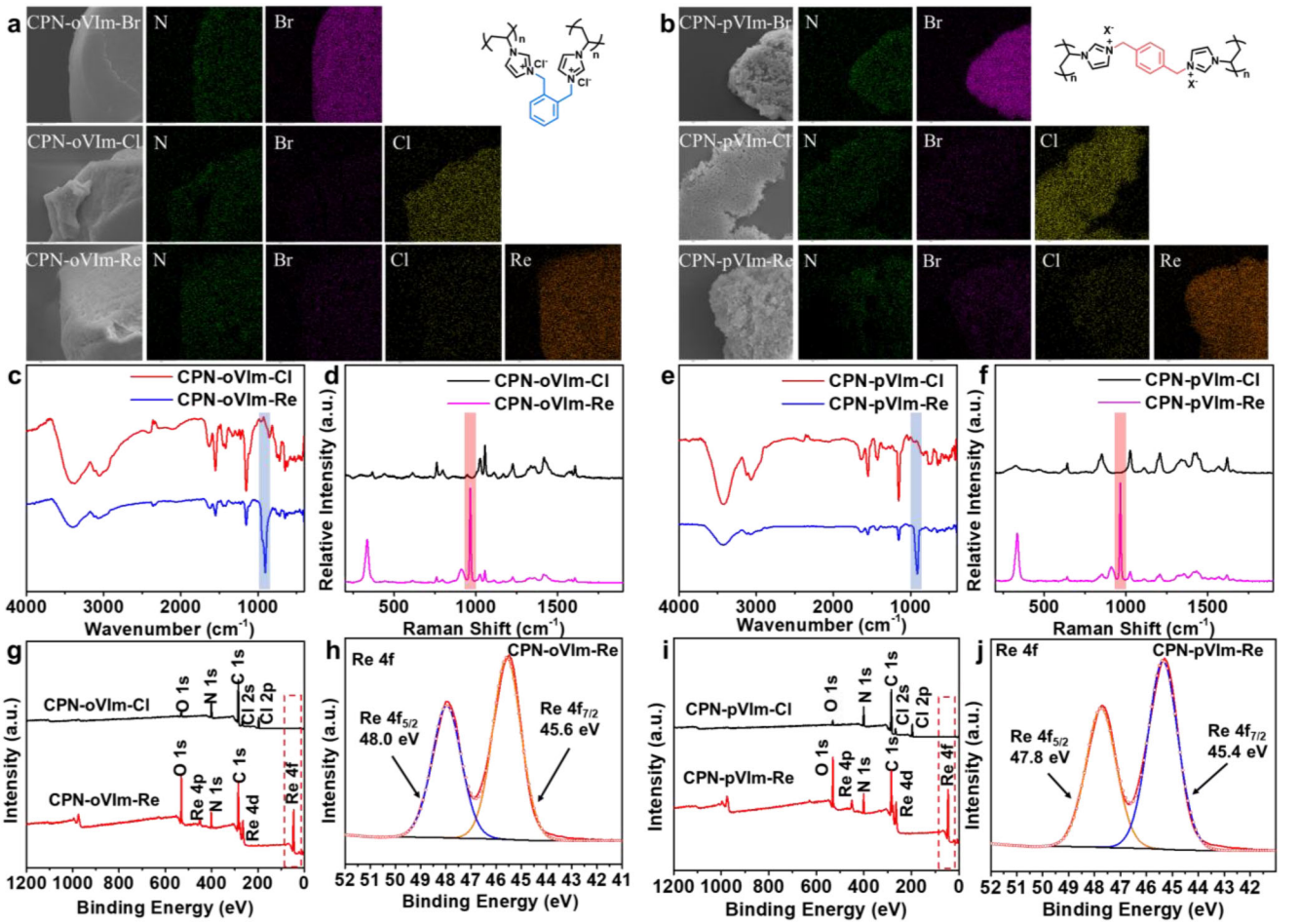


FIGURE 4 | (a) SEM-EDS mapping of **CPN-oVIm-Br**, **CPN-oVIm-Cl**, and **CPN-oVIm-Re**. (b) SEM-EDS mapping of **CPN-pVIm-Br**, **CPN-pVIm-Cl**, and **CPN-pVIm-Re**. FT-IR spectra of (c) **CPN-oVIm** and (e) **CPN-pVIm** before and after anion exchange with ReO_4^-. Characteristic peaks occurring at 910 cm^{-1} (blue band) corresponded to ReO_4^-. Raman spectra of (d) **CPN-oVIm** and (f) **CPN-pVIm** before and after anion exchange with ReO_4^-. Characteristic peaks occurring at 965 cm^{-1} (red band). (g) XPS survey spectra of **CPN-oVIm-Cl** and **CPN-oVIm-Re**. (i) XPS survey spectra of **CPN-pVIm-Cl** and **CPN-pVIm-Re**. XPS analysis of Re 4f from (h) **CPN-oVIm-Re** and (j) **CPN-pVIm-Re**.

while the experimentally determined saturation capacities reach 1221 and 1346 mg g^{-1}, respectively (Table S2). Both experimental values fall slightly below the theoretical maximum of 1377 mg g^{-1}, which assumes the complete utilization of all available ion-exchange sites. Although these capacities are marginally lower than the highest reported values, they remain highly competitive among the various adsorbent materials documented in the literature (see Table S3 for a detailed comparison). At a low initial concentration of 8.5 ppm, **CPN-pVIm-Cl** achieves a removal efficiency exceeding 99.4%, reducing the residual perrhenate concentration to below 50 ppb, which demonstrates its considerable potential for deep-purification applications (Table S4).

Adsorption kinetics constitute a critical metric for assessing the practical efficiency of an adsorbent. The time-dependent uptake of ReO_4^- was investigated by withdrawing aliquots of the solid–liquid mixture at predetermined time intervals and subsequently quantifying the residual rhenium concentration in the supernatant via inductively coupled plasma optical emission spectrometry (ICP-OES). As depicted in Figure 2c,d, both **CPN-pVIm-Cl** and **CPN-oVIm-Cl** display rapid adsorption kinetics, with near-equilibrium conditions attained within 90 min for both materials. Such fast sorption kinetics are highly favorable for the treatment of large volumes of industrial wastewater. The kinetic data were further analyzed using both pseudo-first-order and pseudo-second-order kinetic models. The results demonstrate that the pseudo-second-order model provides a more accurate representation of the adsorption process for both polymers, yielding correlation coefficients (R^2) greater than 0.999 (Figure S7 and Table S5). A comparison of the fitted pseudo-second-order rate constants reveals that **CPN-pVIm-Cl** (k_2 = 5.7×10^{-4} g mg^{-1} min^{-1}) exhibits a somewhat faster initial adsorption rate than **CPN-oVIm-Cl** ($k_2 = 2.0\times10^{-4}$ g mg^{-1} min^{-1}), which may be attributed to the more accessible charge distribution in the *para*-substituted network. The good fit to the pseudo-second-order model indicates that chemisorption, involving ion-exchange interactions between perrhenate anions and the cationic imidazolium sites, is the rate-determining step in the adsorption process.

Given that the pH of real industrial effluents can vary substantially, the influence of solution pH on perrhenate adsorption was investigated across a wide range from 1.7 to 12. As shown in Figure S8, both **CPN-pVIm-Cl** and **CPN-oVIm-Cl** maintain

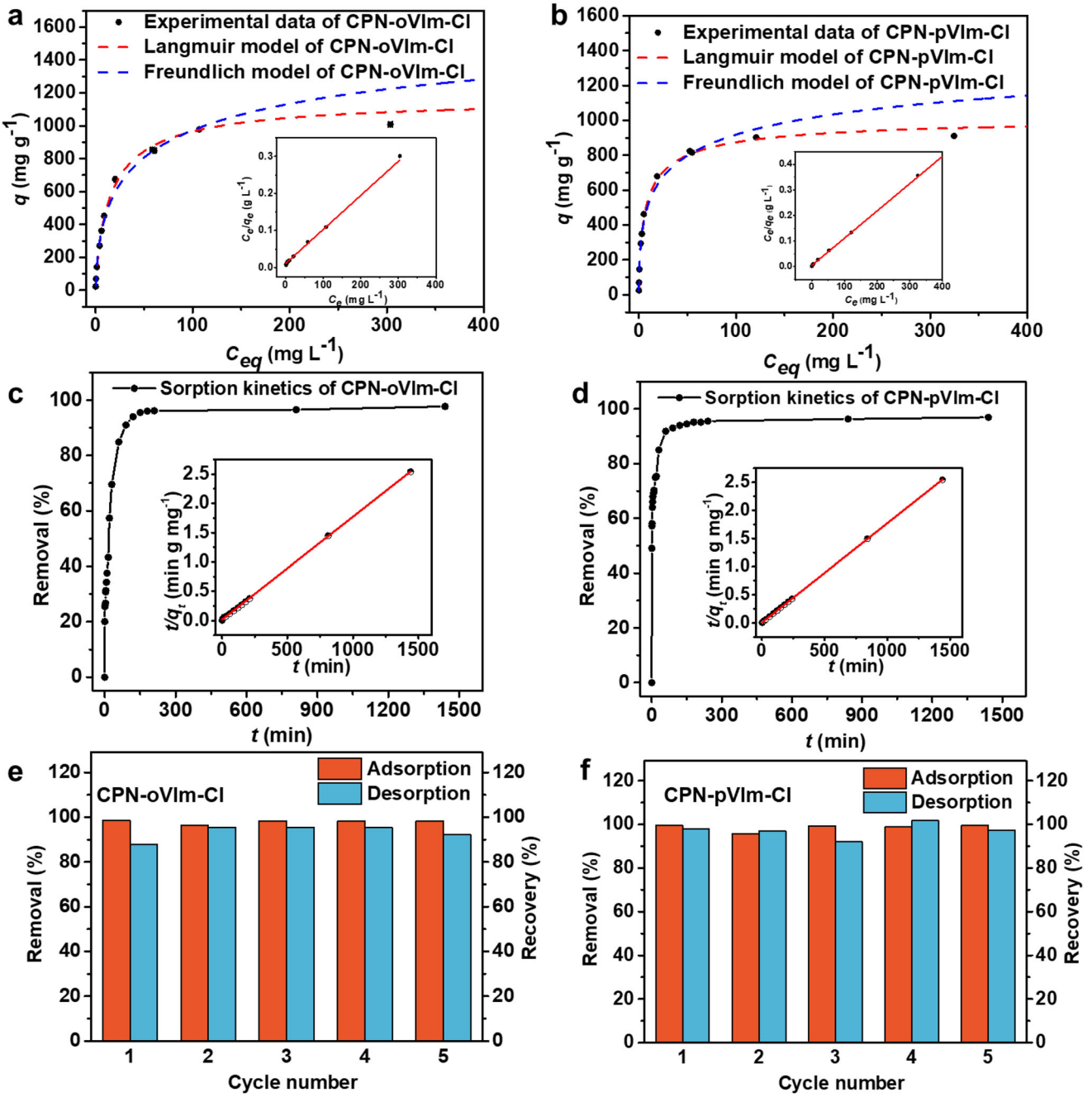


FIGURE 2 | Sorption isotherm of (a) **CPN-oVIm-Cl** and (b) **CPN-pVIm-Cl** for ReO_4^- uptake; the inset shows the fitting curve based on the Langmuir model. Sorption kinetics of (c) **CPN-oVIm-Cl** and (d) **CPN-pVIm-Cl**; the inset shows the fitting curve based on the pseudo-second-order model. Reversibility of (e) **CPN-oVIm-Cl** and (f) **CPN-pVIm-Cl**: red columns show the removal percentages for ReO_4^-, and blue columns show the recovery percentages for ReO_4^-.

relatively high ReO_4^- removal efficiencies throughout this broad pH interval. In particular, the removal rates remain close to 100% within the pH window of 4–10 for both materials, with only a modest decline observed under strongly acidic (pH < 4) or strongly alkaline (pH > 10) conditions. To elucidate the origin of this broad pH tolerance, zeta potential measurements were performed on aqueous dispersions of the two polymers as a function of pH. The results (Figure S9) reveal that both materials maintain positively charged surfaces across the entire tested pH range, which confirms that the cationic nature of the polymers is preserved under diverse acidic and alkaline conditions. This persistent positive surface charge—an intrinsic property of the chemically stable imidazolium-based polymeric framework—underpins the excellent pH adaptability exhibited by both adsorbents.

Reusability represents a crucial performance indicator for evaluating the practical viability of an adsorbent material. Accordingly, consecutive adsorption–desorption cycling tests were carried out for both polymeric materials. As illustrated in Figure 2e,f, after five complete adsorption–desorption cycles, **CPN-pVIm-Cl** retains perrhenate removal and recovery rates of 99.4% and

97.4%, respectively, while **CPN-oVIm-Cl** exhibits comparably stable performance with fifth-cycle removal and recovery rates of 98.2% and 92.1%, respectively. FT-IR spectra acquired before and after five adsorption–desorption cycles show negligible differences (Figure S10), which demonstrates the favorable structural integrity of both **CPN-pVIm-Cl** and **CPN-oVIm-Cl** under repeated cycling conditions. Notably, however, a measurable decline in saturated adsorption capacity is observed after five successive cycles: the capacities of **CPN-pVIm-Cl** and **CPN-oVIm-Cl** decrease to 833 and 861 mg g^{-1}, corresponding to approximately 68% and 64% retention relative to the fresh materials, respectively. This noticeable capacity attenuation is attributed to the cumulative effect of incomplete desorption over repeated adsorption–desorption cycles. Specifically, the desorption efficiency of each individual cycle ranges from 85% to 97% under the current regeneration conditions; consequently, a fraction of the adsorbed perrhenate anions remains tightly bound to the cationic sites and cannot be fully eluted in each cycle. As the number of cycles increases, these incompletely regenerated sites accumulate progressively, ultimately manifesting as a significant reduction in the overall adsorption capacity. The slightly higher capacity retention observed for **CPN-pVIm-Cl** (68%) relative to **CPN-oVIm-Cl** (64%) may be related to the more uniform charge distribution in the *para*-substituted network, which facilitates more efficient ion exchange during both adsorption and desorption processes.

Selective capture in the presence of competing anions is of paramount importance for the treatment of actual smelting wastewater. Mirroring the ionic composition of such industrial effluents, the effects of NO_3^-, SO_4^{2-}, and AsO_4^{3-} on ReO_4^- adsorption were systematically examined for both polymers. In the presence of the monovalent NO_3^- competitor at a 10:1 molar ratio, both polymers maintain high ReO_4^- uptake efficiencies exceeding 95% (Figure 3a,b). By contrast, the introduction of SO_4^{2-} or AsO_4^{3-} at the same molar ratio leads to a more pronounced reduction in uptake (below 90% for **CPN-pVIm-Cl** and below 80% for **CPN-oVIm-Cl**), which underscores the stronger competitive effect exerted by multicharged anions on perrhenate selectivity. To rigorously evaluate the selectivity performance, competition experiments were extended to substantially higher competitor concentrations, with molar ratios of NO_3^-, SO_4^{2-}, and AsO_4^{3-} increased to 1000:1, 5000:1, and 200:1, respectively, to realistically simulate the extreme ionic conditions encountered in actual smelting industrial wastewater. At a 1000:1 ratio of the monovalent NO_3^- competitor, both polymers retain appreciable ReO_4^- uptake, with removal rates of 21.6% for **CPN-pVIm-Cl** and 19.3% for **CPN-oVIm-Cl**. However, the selectivity divergence between the two polymers becomes increasingly pronounced as the charge of the competing anion increases. At an extreme SO_4^{2-}-to-ReO_4^- molar ratio of 5000:1, the ReO_4^- removal rate of the ortho-substituted **CPN-oVIm-Cl** declines to 15.9%, whereas the *para*-substituted **CPN-pVIm-Cl** sustains a markedly higher removal rate of 30.0% (Figure 3c,d). An even more striking contrast is observed for the trivalent AsO_4^{3-} competitor at a 200:1 ratio which the removal rate of **CPN-oVIm-Cl** drops to 42.3%, in sharp contrast to the 71.3% removal rate maintained by **CPN-pVIm-Cl** (Figure 3e,f). This comprehensive set of comparative experiments unequivocally demonstrates that the *para*-substituted **CPN-pVIm-Cl** possesses substantially superior selectivity for ReO_4^- relative to its *ortho*-substituted counterpart, particularly in aqueous environments dominated by high concentrations of multicharged competing anions. To further assess the practical applicability of the materials under realistic industrial conditions, simulated wastewater was prepared based on the chemical composition of copper leach solution from a copper smelting plant in China (detailed in the Supporting Information). The results reveal removal rates of 28.8% and 20.3% for **CPN-pVIm-Cl** and **CPN-oVIm-Cl**, respectively, which further corroborates that **CPN-pVIm-Cl** is more suited for the extraction of rhenium from complex rhenium-containing industrial wastewater.

2.3 | Sorption Mechanism

To gain a detailed understanding of the anion-exchange process occurring between the two cationic polymers and ReO_4^-, a comprehensive mechanistic investigation was undertaken employing multiple complementary analytical techniques, including scanning electron microscopy with energy-dispersive X-ray spectroscopy (SEM-EDS), FT-IR, Raman spectroscopy, and X-ray photoelectron spectroscopy (XPS). The SEM-EDS elemental mapping of the **CPN-pVIm** series provides clear visual evidence of the sequential counterion replacement process (Figure 4b). Upon conversion from **CPN-pVIm-Br** to **CPN-pVIm-Cl**, the bromine signal diminishes markedly while the chlorine signal becomes correspondingly more intense. Subsequent adsorption of ReO_4^- to yield **CPN-pVIm-Re** results in the near-disappearance of the chlorine signal, which is replaced by a well-defined rhenium signal (Figure S11). An analogous sequential ion-exchange progression is observed for the **CPN-oVIm** series, as depicted in Figures 4a and S12. These elemental mapping observations are further corroborated by the XPS survey spectra. As shown in Figure 4g,i, the intensity of the Cl 2p peak decreases substantially following perrhenate adsorption for both polymers, while new peaks attributable to Re 4f concurrently appear in the spectra. Taken together, these results confirm the successful and sequential exchange of counterions from Br^- to Cl^- and ultimately to ReO_4^- in both polymeric systems.

High-resolution XPS analysis was employed to obtain deeper insights into the nature of the adsorptive interactions between the cationic polymers and perrhenate anions. The electronic states of the adsorbed species were examined and compared with those of reference compounds. Figure 4h,j displays the high-resolution Re 4f spectra of both polymers following perrhenate adsorption. Each spectrum can be deconvoluted into two components located at binding energies of approximately 45.5 and 48 eV, which correspond to the Re $4f_{7/2}$ and Re $4f_{5/2}$ doublet characteristic of Re(VII) in the perrhenate oxidation state [23]. A more refined comparison reveals measurable differences in binding energy shifts when the spectra are referenced against that of standard $NaReO_4$. Specifically, both the Re $4f_{7/2}$ and Re $4f_{5/2}$ peaks of **CPN-oVIm-Re** exhibit a shift of approximately 0.4 eV relative to NaReO4, whereas a larger shift of about 0.6 eV is observed for **CPN-pVIm-Re**. Furthermore, analysis of the N 1s core-level spectra reveals that the N 1s peak of **CPN-oVIm** shifts by approximately 0.2 eV following perrhenate adsorption, while the corresponding shift for **CPN-pVIm** is approximately 0.3 eV (Figure S13 and Table S6) [24, 25]. The consistently larger binding energy shifts observed for both Re 4f and N 1s in the *para*-substituted **CPN-pVIm-Re** relative to the *ortho*-substituted **CPN-oVIm-Re** are indicative

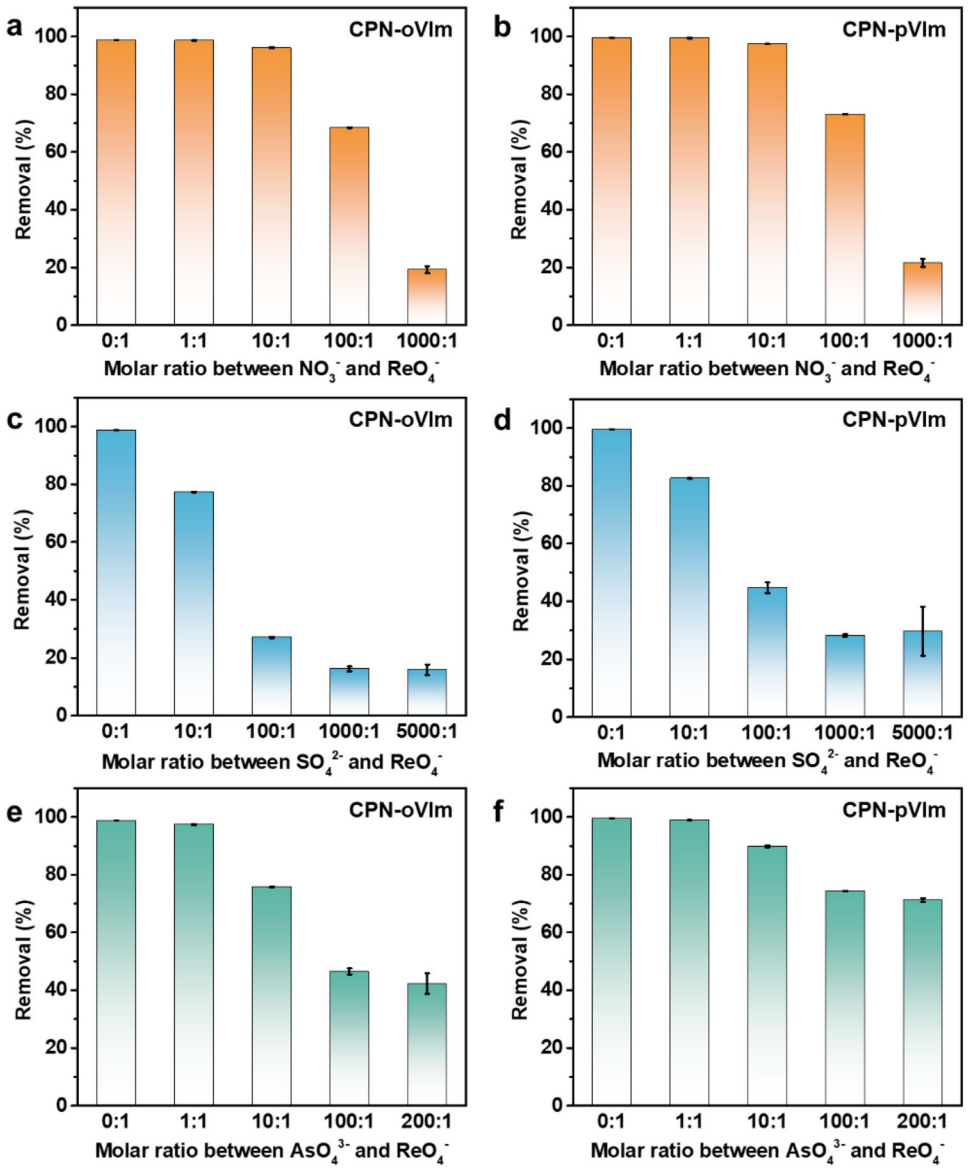


FIGURE 3 | Effect of competing NO_3^- on the anion exchange of ReO_4^- by (a) **CPN-oVIm-Cl** and (b) **CPN-pVIm-Cl**. Effect of competing SO_4^{2-} on the anion exchange of ReO_4^- by (c) **CPN-oVIm-Cl** and (d) **CPN-pVIm-Cl**. Effect of competing AsO_4^{3-} anions on the anion exchange of ReO_4^- by (e) **CPN-oVIm-Cl** and (f) **CPN-pVIm-Cl**.

of a stronger electronic interaction between the imidazolium cationic sites and the adsorbed perrhenate anions in the para-configuration. This enhanced electronic interaction is consistent with the more uniform charge distribution in **CPN-pVIm-Cl** and correlates directly with its superior selectivity for ReO_4^- capture in competitive environments.

In addition, vibrational spectroscopic techniques provide molecular-level evidence for the capture of ReO_4^-. The FT-IR spectra presented in Figure 4c,e reveal that a new absorption band appears near 910 cm^{-1} for both **CPN-pVIm-Cl** and **CPN-oVIm-Cl** following perrhenate adsorption [26]. This band is assignable to the asymmetric stretching vibration of the ReO_4^- anion. Likewise, the Raman spectra shown in Figure 4d,f exhibit a new resonance at 965 cm^{-1} after adsorption, which constitutes an additional spectroscopic fingerprint of ReO_4^-. Importantly, the characteristic spectral features associated with the imidazolium polymer backbone remain well preserved after adsorption, confirming that the ion-exchange process does not compromise the structural integrity of the polymer networks. Integrating the full suite of characterization results enables a coherent mechanistic explanation for the observed selectivity difference between the two polymers. The fundamental origin of this divergence lies in the distinct spatial arrangements of the cationic functional groups. In the *ortho*-substituted **CPN-oVIm-Cl**, the two imidazolium cations are situated in close proximity on the phenylene linker. This adjacency gives rise to localized clustering of positive charge, thereby creating regions of elevated charge density within the polymer network. Such an electrostatic landscape exerts a stronger but less discriminating attractive force toward anions carrying higher negative charge. Consequently, in the presence of multicharged competing anions, the selectivity toward the monovalent target ReO_4^- is diminished. In contrast, in the *para*-substituted

CPN-pVIm-Cl, the cationic groups are positioned at opposite ends of the phenylene linker. This configuration maximizes their spatial separation, resulting in a more homogeneous and evenly dispersed distribution of positive charge throughout the polymer network. This uniform electrostatic environment mitigates the excessive nonspecific capture of multivalent ions while simultaneously favoring the geometric compatibility and specific recognition of the target ReO_4^- anion, thereby leading to significantly enhanced selectivity. Through rational molecular design and comprehensive multi-technique characterization, this work definitively establishes the spatial geometry of cationic functional groups as a key intrinsic parameter governing ion-exchange selectivity in cationic polymeric adsorbents.

3 | Conclusion

In summary, the present study systematically investigates the influence of functional group spatial arrangement on anion selectivity through the rational design of two imidazolium-based cationic polymers with *ortho*- and *para*-disubstituted configurations (**CPN-oVIm-Cl** and **CPN-pVIm-Cl**) for perrhenate capture. While both materials demonstrate high adsorption capacities (up to 1346 mg g^{-1}), rapid sorption kinetics (> 90% removal within 90 min), broad pH adaptability (near-complete removal between pH 4 and 10), and stable reusability over five consecutive cycles, the central finding of this work lies in the pronounced selectivity divergence between the two regioisomeric polymers. The *para*-substituted **CPN-pVIm-Cl** significantly outperforms its *ortho*-substituted counterpart in aqueous environments containing high concentrations of multicharged competing anions such as SO_4^{2-} and AsO_4^{3-}, as validated by both systematic competition experiments and tests under simulated industrial wastewater conditions. Mechanistic investigations attribute this superior selectivity to the more homogeneous charge distribution characteristic of the *para*-substituted architecture, which enhances specific recognition of the monovalent target ReO_4^- anion while suppressing nonspecific binding of multivalent competitors. This study conclusively establishes the spatial arrangement of cationic functional groups as a pivotal and tunable design parameter for governing ion-exchange selectivity in cationic polymers. Beyond the performance demonstration of individual adsorbent materials, the findings provide a valuable molecular-level design rationale and a novel structural engineering strategy for the development of high-performance separation materials tailored to complex multicomponent ionic systems.

Author Contributions

Xiaorui Li: data curation, methodology, investigation, validation, writing – original draft. **Jiahong Yang**: investigation, data curation. **Wenping Liu**: investigation, data curation. **Haiying Wang**: supervision, investigation, data curation. **Yu Zhang**: investigation, data curation. **Xinhui Deng**: investigation. **Linfeng Jin**: investigation, data curation. **Huan Li**: data curation. **Changqing Su**: investigation. **Yiming Li**: conceptualization, funding acquisition, project administration, supervision, resources, writing – review and editing. **Thamraa AlShahrani**: Resources, funding acquisition. **Shengqian Ma**: conceptualization, supervision, funding acquisition, writing – review and editing.

Acknowledgments

The authors acknowledge the financial support received from the National Natural Science Foundation of China (52304421), National Key Research and Development Program (2022YFC3900902, 2024YFC3907902), Scientific Research Fund of Hunan Provincial Education Department (25B0571, 23B0601), Hunan Science and Technology Innovation Plan (2024RC3015), Natural Science Foundation of Hunan Province (2023JJ40230) and Major Science and Technology Special Project of Changsha (KH2301012). Partial support from the Robert A. Welch Foundation (B-0027) (S.M.) and Princess Nourah Bint Abdulrahman University Researchers Supporting Project (PNURSP2026R1), Riyadh, Saudi Arabia is also acknowledged (T.A.).

Conflicts of Interest

The authors declare no conflicts of interest.

Data Availability Statement

The data that support the findings of this study are available from the corresponding author upon reasonable request.

Use of Generative AI and AI-Assisted Technologies in the Writing Process

During the preparation of this manuscript, no artificial intelligence (AI) tools were used to generate or substantially rewrite the scientific content. Any AI-assisted language editing was limited to grammatical and stylistic polishing of the authors' original text, and all scientific content, data interpretation, and conclusions were generated exclusively by the authors. The authors take full responsibility for the integrity and originality of the work.

References

1. *Mineral Commodity Summaries, 2025*, (U.S. Geological Survey, 2025), 212.

2. D.-W. Fang, W.-J. Shan, Q. Yan, D. Li, L.-X. Xia, and S.-L. Zang, "Extraction of Rhenium From Sulphuric Acid Solution With Used Amine N235," *Fluid Phase Equilibria* 383 (2014): 1–4, https://doi.org/10.1016/j.fluid.2014.09.012.

3. H. S. Kim, J. S. Park, S. Y. Seo, T. Tran, and M. J. Kim, "Recovery of Rhenium From a Molybdenite Roaster Fume as High Purity Ammonium Perrhenate," *Hydrometallurgy* 156 (2015): 158–164, https://doi.org/10.1016/j.hydromet.2015.06.008.

4. H. Hu, S. Yu, T. Wang, H. Lian, and C. Lv, "Recovery of Rhenium, a Strategic Metal, From Copper Smelting Effluent," *Separation and Purification Technology* 337 (2024): 126403, https://doi.org/10.1016/j.seppur.2024.126403.

5. X. Li, Y. Li, H. Wang, et al., "3D cationic Polymeric Network Nanotrap for Efficient Collection of Perrhenate Anion From Wastewater," *Small* 17 (2021): 2007994, https://doi.org/10.1002/smll.202007994.

6. J. Li, X. Dai, L. Zhu, et al., "$^{99}TcO_4^-$ Remediation by a Cationic Polymeric Network," *Nature Communications* 9 (2018): 3007, https://doi.org/10.1038/s41467-018-05380-5.

7. D. Sheng, L. Zhu, X. Dai, et al., "Successful Decontamination of $^{99}TcO^-$ in Groundwater at Legacy Nuclear Sites by a Cationic Metal-Organic Framework With Hydrophobic Pockets," *Angewandte Chemie International Edition* 58 (2019): 4968–4972, https://doi.org/10.1002/anie.201814640.

8. M. Lei, M. Hao, Z. Chen, et al., "Designing Metal-Organic Frameworks for the Selective Removal of $^{99}TcO_4^-$ From Nuclear Wastewater," *Science China Chemistry* 68 (2025): 1639–1641, https://doi.org/10.1007/s11426-025-2556-y.

9. L. He, S. Liu, L. Chen, et al., "Mechanism Unravelling for Ultrafast and Selective $^{99}TcO^-$ Uptake by a Radiation-Resistant Cationic Covalent

Organic Framework: A Combined Radiological Experiment and Molecular Dynamics Simulation Study," *Chemical Science* 10 (2019): 4293–4305, https://doi.org/10.1039/C9SC00172G.

10. Q. Sun, L. Zhu, B. Aguila, et al., "Optimizing Radionuclide Sequestration in Anion Nanotraps With Record Pertechnetate Sorption," *Nature Communications* 10 (2019): 1646, https://doi.org/10.1038/s41467-019-09630-y.

11. X. Zhang, M. Hao, X. Yang, et al., "Promising Porous Materials for $^{99}TcO_4^-$ Removal From Nuclear Wastes," *National Science Open* 4 (2024): 20240007, https://doi.org/10.1360/nso/20240007.

12. H. Hu, L. Sun, Y. Gao, et al., "Synthesis of ZnO Nanoparticle-Anchored Biochar Composites for the Selective Removal of Perrhenate, a Surrogate for Pertechnetate, From Radioactive Effluents," *Journal of Hazardous Materials* 387 (2019): 121670, https://doi.org/10.1016/j.jhazmat.2019.121670.

13. Z. Sun, Y. Liao, Y. Zhang, et al., "Sustainable Carbon Materials in Environmental and Energy Applications," *Sustainable Carbon Materials* 1 (2025): e007, https://doi.org/10.48130/scm-0025-0002.

14. J. Tong, B. Chang, B. Li, et al., "Separation of ^{99}Tc by Ion Exchange Martials: A Critical Review," *Journal of Environmental Chemical Engineering* 13 (2025): 117349, https://doi.org/10.1016/j.jece.2025.117349.

15. K. O. Ojima, S. H. Dayarathne, M. T. Kelly, and B. Zhao, "Quaternary Ammonium-Containing Polyelectrolyte Brush Particles for Removal of Perrhenate Anion From Water: Effect of N-Substituents," *Macromolecular Rapid Communications* 46 (2025): 2401087, https://doi.org/10.1002/marc.202401087.

16. M. Shi, D. Chen, X. Zhao, Y. Tian, and R. Zhao, "Converting Nonporous Cationic Polymeric Networks to Cationic Porous Aromatic Frameworks for Enhanced $^{99}TcO_4^-/ReO_4^-$ Elimination," *Separation and Purification Technology* 352 (2025): 128194, https://doi.org/10.1016/j.seppur.2024.128194.

17. M. Shi, D. Chen, X. Zhao, et al., "Robust and Porous Cationic Polymeric Network Nanofiber Membrane With High Alkaline Stability for Efficient $^{99}TcO_4^-/ReO_4^-$ Removal," *Chemical Engineering Journal* 506 (2025): 160140, https://doi.org/10.1016/j.cej.2025.160140.

18. J. Li, B. Li, N. Shen, et al., "Task-Specific Tailored Cationic Polymeric Network With High Base-Resistance for Unprecedented^{99} TcO– Cleanup From Alkaline Nuclear Waste," *ACS Central Science* 7 (2021): 1441–1450, https://doi.org/10.1021/acscentsci.1c00847.

19. W. Wu, X. Liu, X. Yang, et al., "Facile Synthesis of Imidazolium Cationic Organic Polymer With Ultrafast $ReO_4^-/^{99}TcO_4^-$ Removal Under Highly Alkaline Conditions," *Separation and Purification Technology* 318 (2023): 123951, https://doi.org/10.1016/j.seppur.2023.123951.

20. L. S. Pang, X. Liao, C. Y. Zhao, C. P. Li, Z. Liu, and S. Ma, "From Radioactive Effluent to Drinking Water: Efficient Removal of Trace^{99} TcO^-/ReO^- by Cationic Porous Aromatic Framework," *Advanced Science* 12 (2025): 2414604, https://doi.org/10.1002/advs.202414604.

21. X. Li, W. Liu, H. Wang, et al., "Efficient Capture of ReO^- From Water by Imidazolium-Based Cationic Polymeric Nanotraps," *Chemistry—An Asian Journal* 20 (2025): e202401419, https://doi.org/10.1002/asia.202401419.

22. X. Li, L. Jin, L. Huang, et al., "Imidazolium-Based Cationic Polymeric Nanotraps for Efficient Removal of $Cr_2O_7^{2-}$," *Journal of Environmental Chemical Engineering* 9 (2021): 106357, https://doi.org/10.1016/j.jece.2021.106357.

23. Z. W. Liu and B. H. Han, "Evaluation of an Imidazolium-Based Porous Organic Polymer as Radioactive Waste Scavenger," *Environmental Science & Technology* 54 (2020): 216–224, https://doi.org/10.1021/acs.est.9b05308.

24. L. Chen, X. Yin, Q. Yu, et al., "Rapid and Selective Capture of Perrhenate Anion From Simulated Groundwater by a Mesoporous Silica-Supported Anion Exchanger," *Microporous and Mesoporous Materials* 274 (2019): 155–162, https://doi.org/10.1016/j.micromeso.2018.07.029.

25. Y. Xie, J. Lin, H. Lin, et al., "Removal of Anionic Hexavalent Chromium and Methyl Orange Pollutants by Using Imidazolium-Based Mesoporous Poly(Ionic Liquid)s as Efficient Adsorbents in Column," *Journal of Hazardous Materials* 392 (2020): 122496, https://doi.org/10.1016/j.jhazmat.2020.122496.

26. J. Tong, Y. Liu, L. Han, et al., "Construction of a Porous Zwitterionic Polyimidazole Resin for the Elimination of Technetium in Acidic Environments," *ACS Applied Materials & Interfaces* 17 (2025): 21323–21334, https://doi.org/10.1021/acsami.5c02697.

Supporting Information

Additional supporting information can be found online in the Supporting Information section.

This section provides a detailed account of the synthesis, characterization, adsorption experiments, and supplementary evidence supporting the partial adsorption mechanism.

Supporting File: asia70995-sup-0001-SuppMat.docx.